



2D Co-incorporated hydroxyapatite nanoarchitecture as a potential efficient oxygen evolution cocatalyst for boosting photoelectrochemical water splitting on Fe_2O_3 photoanode



Ruifeng Chong^a, Yuqing Du^a, Zhixian Chang^{a,*}, Yushuai Jia^b, Yan qiao^c, Shanhui Liu^d, Yong Liu^a, Yanmei Zhou^d, Deliang Li^{a,*}

^a Institute of Upconversion Nano-scale Materials, College of Chemistry and Chemical Engineering, Henan University, Kaifeng, 475004, China

^b Institute of Advanced Materials, College of Chemistry and Chemical Engineering, Jiangxi Normal University, Nanchang, 330022, China

^c Department of Pathophysiology, Basic Medical College of Zhengzhou University, Zhengzhou, 450001, China

^d Henan Joint International Research Laboratory of Environmental Pollution Control Materials, College of Chemistry and Chemical Engineering, Henan University, Kaifeng, 475004, China

ARTICLE INFO

Keywords:

Co-incorporated hydroxyapatite
Hematite
Water oxidation
Photoelectrochemical
Neutral electrolyte

ABSTRACT

The serious charge recombination together with the sluggish water oxidation kinetics have largely limited the practical application of hematite (Fe_2O_3) in photoelectrochemical (PEC) water splitting. Surface modification with oxygen evolution cocatalyst is an efficient strategy to address the both issues. Herein, a novel 2D oxygen evolution cocatalyst, namely Co-incorporated hydroxyapatite (Co-HAP) nanoarchitecture, was rationally designed and decorated on Fe_2O_3 photoanode. The resulting Co-HAP decorated Fe_2O_3 (Co-HAP/ Fe_2O_3) exhibited excellent PEC water splitting with a high photocurrent density of 2.25 mA cm^{-2} at 1.23 V vs. RHE in neutral electrolyte, which is *ca.* 9.78 times that for bare Fe_2O_3 . Moreover, the onset potential displayed a 200 mV cathodic shift, indicating an accelerated water oxidation kinetics over Fe_2O_3 . PEC characterizations revealed Co-HAP could not only significantly improve the charge-separation efficiency but also could enhance the surface charge-separation efficiency in the bulk and on the surface of Fe_2O_3 . Comprehensive investigations unveiled the interfacial negative electrostatic field and the increased electrical conductivity arising from Co-HAP decoration were of great benefit to improve the charge separation and inhibit surface charge recombination, while the 2D architecture of Co-HAP offered high surface area and abundant exposed Co active sites, ultimately boosted PEC water splitting over Fe_2O_3 . Owing to the superior ion-exchange ability of HAP, the strategy presented here would open a new vane to explore highly efficient oxygen evolution cocatalyst.

1. Introduction

Photoelectrochemical (PEC) water splitting, using renewable solar irradiation and water as energy sources to produce H_2 , provides a clean and sustainable strategy for future energy demands [1,2]. Due to the kinetically sluggish process, the oxygen evolution reaction (OER) is usually considered as a critical half-reaction for overall water splitting [3,4]. Therefore, the efficient and robust photoanodes are highly desired to achieve the conversion from solar energy to H_2 energy. To date, various n-type semiconductors, such as TiO_2 , ZnO , BiVO_4 , Ta_2N_5 , WO_3 and Fe_2O_3 , have been applied as photoanode materials to optimize PEC performance for water oxidation [5–7]. Among them, the abundant and ecofriendly Fe_2O_3 with a suitable bandgap of 1.9–2.2 eV and a high absorption range of *ca.* 40% solar radiation was considered as an

attractive candidate [8]. Theoretically, the maximum solar-to-hydrogen efficiency over Fe_2O_3 could reach 15.3%, corresponding to a photocurrent density of *ca.* 12.6 mA cm^{-2} at 1.23 V vs. RHE under AM 1.5 G. However, the inherent drawbacks of Fe_2O_3 in terms of the short hole diffusion length ($L_D \sim 2\text{–}4 \text{ nm}$) and poor conductivity results in the lifetime of photogenerated carriers in Fe_2O_3 on picosecond scale, which is far below the milliseconds required for drive efficient water oxidation [9,10].

To address the above challenges, many approaches including structural control, heterojunction construction [11,12], bulk doping [13,14], and surface modification [15] have been well developed. Among these strategies, surface modification with oxygen evolution cocatalyst (OECs) is one of the most effective strategies to improve the interfacial hole extraction kinetics, that is, prolong the lifetime of

* Corresponding authors.

E-mail addresses: chzx19@henu.edu.cn (Z. Chang), lideliang@henu.edu.cn (D. Li).

photogenerated carriers, and simultaneously decrease the overpotential of water oxidation, thus accelerating the surface oxygen evolution kinetics over Fe_2O_3 [16,17]. For example, Ru- and Ir-based oxides demonstrated excellent ability that enhanced PEC water splitting over Fe_2O_3 [18,19]. However, the low abundance and high cost limited their large-scale application. Recently, a tremendous attraction was focused on the exploration of inexpensive and earth-abundant cobalt- and nickel-based OECs to modify Fe_2O_3 -based photoanodes [20–22], and a series of encouraging results have been achieved. As an outstanding OEC, cobalt-phosphate complexes (Co-Pi) could effectively capture and store photogenerated holes from Fe_2O_3 through the conversion of Co(II) into high-valence Co(III) or Co(IV), thus enhance the charge separation, prolong the carriers' lifetime and provide active sites for water oxidation [23]. Moreover, phosphate anion acted as an effective linker between Fe_2O_3 surface and Co active sites. However, the most commonly used photo-assisted electrodeposition of CoPi still suffered from insufficient charge accumulation due to a barrier or incomplete physical contact between the semiconductor and CoPi layer [23]. The engineering of CoPi-like species on semiconductor is therefore essential to explore highly efficient OECs for PEC water splitting.

Calcium hydroxyapatite ($\text{Ca}_{10}(\text{PO}_4)_6(\text{OH})_2$, HAP), a stable apatite compound, has a hexagonal structure consisting of Ca^{2+} sites by PO_4^{3-} tetrahedron and OH- groups. Due to excellent ion-exchange ability, large adsorption capacity, high surface area and unique acid-base character, HAP has been widely used in the fields of biomedicine and catalysis [24–26]. The exchange of Ca^{2+} in HAP with various divalent, trivalent or quadrivalent cations would lead to high dispersion of metal cations in HAP lattice and endow novel function to HAP. For example, ion-doped HAP showed obvious antibacterial activity with increased mechanical strength, surface roughness and dielectric property [27]. Wei reported incorporation of magnetic ions (Fe, Co and Ni) into HAP lattice was sufficient to induce a transition from the diamagnetic behavior to a paramagnetic one [28]. Ni-HAP and Co-HAP also exhibited good activity and high selectivity toward water-gas shift reaction [29]. Inspired by such results combined with superior OEC activity of CoPi, Co-HAP is thus speculated to be a potential OEC with high efficiency for PEC water oxidation.

In this work, 2D Co-HAP nanoarchitectures were successfully decorated on Fe_2O_3 nanorod arrays *via* an in-situ growth followed by ionic-exchange strategy. PEC measurements indicated 2D Co-HAP possessed excellent catalytic performance that enhanced the PEC water splitting over Fe_2O_3 in neutral electrolyte. The photocurrent density of Co-HAP/ Fe_2O_3 reached an altitude of 2.25 mA cm^{-2} at 1.23 V (vs. RHE), which was approximately 9.78-, 2.32- and 2.78- fold of Fe_2O_3 , HAP/ Fe_2O_3 and CoPi/ Fe_2O_3 . Moreover, Co-HAP/ Fe_2O_3 exhibited a lower onset potential with *ca.* 200 mV cathodic shift than that of Fe_2O_3 . Experimental studies indicated Co-HAP not only could improve the charge separation and inhibit surface charge recombination but also supply abundant exposed Co active sites, thus boost PEC water oxidation over Fe_2O_3 .

2. Experimental

2.1. Preparation of HAP/ Fe_2O_3 and Co-HAP/ Fe_2O_3 photoanodes

The Fe_2O_3 film was prepared by using our previous method [21,27]. Typically, 15 mmol $\text{FeCl}_3 \cdot 6\text{H}_2\text{O}$ (4.055 g) and 15 mmol urea (0.9008 g) were dissolved into 50 mL high purity water in a glass beaker, followed by Fluorine doped tin oxide (FTO) glass was placed vertically in the beaker with the conducting surface facing wall. Then the beaker was heated at 100 °C for 6 h. After being cooled naturally, the film on FTO was washed with high purity water for three times and then was annealed at 500 °C for 3 h followed by 750 °C for 15 min.

For preparation of HAP/ Fe_2O_3 , $\text{Ca}(\text{OH})_2$ was first deposited on Fe_2O_3 . In typical, Fe_2O_3 film was immersed in 100 mL room temperature saturated $\text{Ca}(\text{OH})_2$ solution under Ar at 100 °C for 30, 60 and

90 min, and then the film was washed thoroughly with ethanol and dried in vacuum for 60 min. The resulting $\text{Ca}(\text{OH})_2/\text{Fe}_2\text{O}_3$ was subsequently placed in 50 mL autoclave containing 20 mL 0.1 mol L^{-1} $(\text{NH}_4)_2\text{HPO}_4$ (pH = 10, adjusted by 1 mol L^{-1} NaOH) and heated to 120 °C and kept for 10 h. According to the immersion time (30, 60 and 90 min) for deposition of $\text{Ca}(\text{OH})_2$, the as-obtained HAP/ Fe_2O_3 were denoted as HAP/ Fe_2O_3 -1, HAP/ Fe_2O_3 -2 and HAP/ Fe_2O_3 -3, respectively. Co-HAP/ Fe_2O_3 was prepared by using ion-exchange method with the representative HAP/ Fe_2O_3 -2. In detail, HAP/ Fe_2O_3 -2 was immersed in 50 mL 0.01 mol L^{-1} $\text{Co}(\text{NO}_3)_2$ solution at 40 °C for 40 min.

For comparison, Co-HAP/ Fe_2O_3 -N was also prepared a direct hydrothermal method. Typically, HAP/ Fe_2O_3 -N was first fabricated by placing Fe_2O_3 directly in a mixture of 20 mL 0.1 mol L^{-1} $(\text{NH}_4)_2\text{HPO}_4$ and 10 mL saturated $\text{Ca}(\text{OH})_2$ and then kept 120 °C for 10 h in an autoclave. The HAP/ Fe_2O_3 -N was immersed in $\text{Co}(\text{NO}_3)_2$ solution to prepare Co-HAP/ Fe_2O_3 -N, as that for Co-HAP/ Fe_2O_3 . For preparation of CoPi/ Fe_2O_3 film, Co-Pi was photo-assisted electrodeposition onto the Fe_2O_3 by modification of published procedures. Briefly, a three-electrode cell was used with Fe_2O_3 as the working electrode, the saturated Hg/HgCl_2 as the reference electrode, and Pt plate as the counter electrode. The electrolyte was prepared with 0.5 mM cobalt nitrate in 0.1 M pH 7 potassium phosphate (KPi) buffer. Co-Pi was photoelectrodeposited at 1.23 V vs. RHE for 15 min under illumination with a 300 W xenon lamp (100 mW cm^{-2}) [23,28].

2.2. (Photo)electrochemical measurements

PEC measurements were performed on a CHI 760E electrochemical workstation with a three-electrode configuration using Hg/HgCl_2 in sat. KCl as reference electrode, Pt wire as counter electrode and the prepared films with an active area *ca.* 0.12 cm^2 as working electrodes. The electrolyte was 0.5 mol L^{-1} sodium phosphate buffer (Na-Pi, pH = 7). The light source was a 300 W xenon lamp (PLS-SXE300CUV, Perfectlight Techn. Co. Ltd., Beijing). The intensity of light source was calibrated to 100 mW cm^{-2} . The potentials were calibrated with respect to the reversible hydrogen electrode (RHE) using the equation of $E_{\text{RHE}} = E_{\text{SCE}} + 0.244 \text{ V} + 0.059 \text{ V} \times \text{pH}$. The photocurrent was recorded by using linear sweep voltammetry (LSV) with a scan rate of 20 mV s^{-1} .

Electrochemical Impedance Spectra (EIS) were conducted on CHI 760E electrochemical workstation at a DC potential of 1.23 V (vs. RHE) and an AC potential frequency range of 100,000–0.1 Hz with an amplitude of 10 mV under illumination. The electrochemically active surface area (ECSA) was estimated from electrochemical double-layer capacitance (C_{dl}) by using cyclic voltammograms (CVs) in a non-Faradaic region (0.56–0.86 V vs. RHE).

2.3. PEC water splitting evaluation

PEC water splitting for O_2 and H_2 evolution was performed in a three-electrode cell connected to a closed gas circulation and evacuation system. Co-HAP/ Fe_2O_3 (2 cm × 3 cm) as working electrode, Pt plate (2 cm × 2 cm) with a distance of 5 cm and Hg/HgCl_2 in sat. KCl as reference electrode were immersed in 80 mL of 1 mol L^{-1} sodium phosphate buffer (Na-Pi, pH = 7). The working electrode was applied a bias of 1.23 V vs. RHE and irradiated by a 300 W Xe lamp (100 mW cm^{-2}). The PEC cell was maintained at 20 ± 0.5 °C by a cooling water bath during the reaction. Evolved O_2 and H_2 were analyzed by an online gas chromatograph with thermal conductivity detector (Tianmei GC 7890, 5 Å zeolite column and Ar carrier gas).

3. Results and discussion

3.1. Preparation and characterizations for Co-HAP/ Fe_2O_3

The procedure for the fabrication of Co-HAP/ Fe_2O_3 photoanode is schematically illustrated in Fig. 1, which is a combination of in-situ

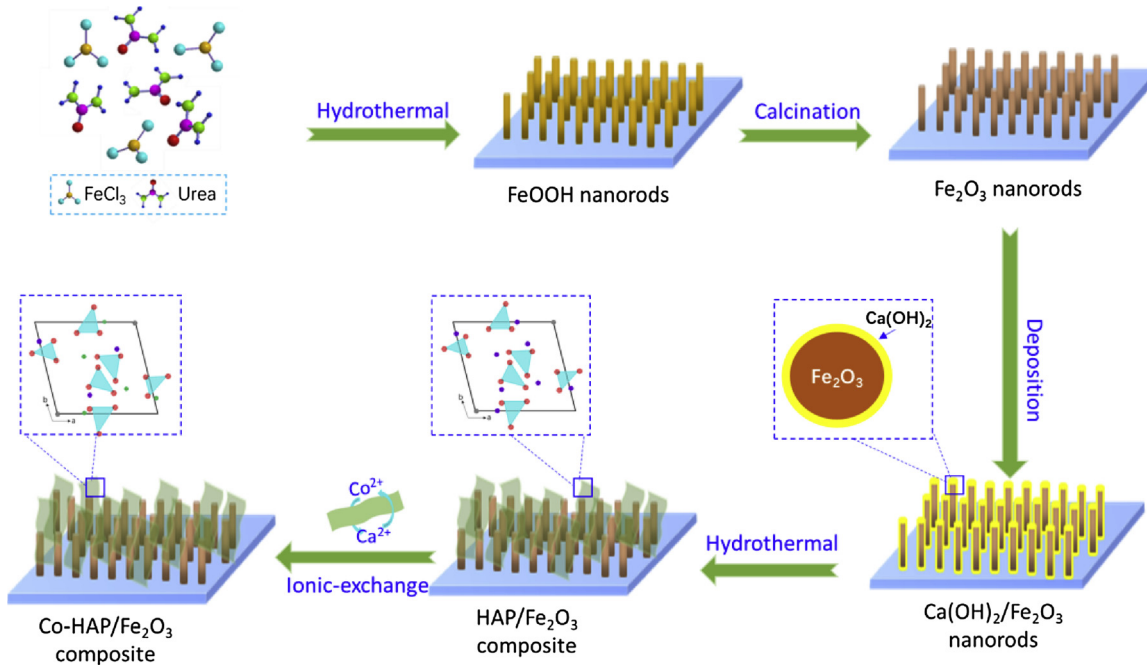


Fig. 1. Schematic illustration for the fabrication of Co-HAP/Fe₂O₃.

deposition, in-situ growth and ion-exchange process. Namely, Ca(OH)₂ was first deposited on Fe₂O₃ in saturated Ca(OH)₂ solution and then in-situ reacted with (NH₄)₂HPO₄ to form HAP/Fe₂O₃, and finally partial Ca was ion-exchanged by Co. The obtained samples were first examined by using scanning electron microscopy (SEM) and shown in Fig. 2a-d. Fig. 2a shows the individual grain of pristine Fe₂O₃ is rod-like and without any changes after being deposited with Ca(OH)₂ (Fig. 2b). As for HAP/Fe₂O₃, obvious 2D graphene-like network was vertically oriented on Fe₂O₃ (Fig. 2c), indicated Ca(OH)₂ precursor underwent a dissolution-reprecipitation process during the formation of HAP. After being ion-exchanged with Co, no distinguishable differences in terms of morphology and sizes were observed (Fig. 2d), indicative of a stable structure of HAP. Such architecture of Co-HAP is expected to have potential to provide much more active sites, maximize electro-chemically active surface area and offer large electrode/electrolyte interface. Elemental mapping images demonstrate Ca, P and Co are uniformly distributed over Fe₂O₃ (Fig. 2e and Fig. S1), suggesting Co species are well dispersed throughout HAP. In contrast, HAP/Fe₂O₃-N shows irregular HAP with serious agglomerations scattered on Fe₂O₃ (Fig. S2), indicating the pre-deposition of Ca(OH)₂ is essential for the decoration of 2D Co-HAP with highly dispersed Co species.

Fig. 3a-h comparably exhibit the surface and cross-sectional SEM images of bare Fe₂O₃, HAP/Fe₂O₃-1, HAP/Fe₂O₃-2 and HAP/Fe₂O₃-3. Apparently, the deposition of HAP is highly dependent on the deposition time of Ca(OH)₂. Prolong the deposition time of Ca(OH)₂ would cause larger amount of HAP deposit. Fig. 3e shows the thickness of pristine Fe₂O₃ is ~200 nm, which is of no change after being deposited with Ca(OH)₂ (Fig. S3). Elemental mapping for Ca of Ca(OH)₂/Fe₂O₃ in Fig. S3 indicates Ca(OH)₂ is uniformly dispersed throughout the whole Fe₂O₃ nanorods. A visible HAP overlayer was observed with increased thickness from ~25 to 200 nm as the prolonging deposition time of Ca(OH)₂ from 30 to 90 min (Fig. 3f-h). Transmission electron microscopy (TEM) was further used to provide more insights on the morphology transformation from Fe₂O₃ to Ca(OH)₂/Fe₂O₃ and then to HAP/Fe₂O₃ (Fig. S4 and Fig. 3i-k). As seen, Fe₂O₃ possesses a smooth surface, which are coated with a uniform film with the thickness of ~5–15 nm after being deposited with Ca(OH)₂. Interestingly, a clear 2D architecture of HAP with an edge thickness ~6 nm are scattered on the surface of Fe₂O₃ (Fig. 3i and j), which further suggests the formation of HAP via a

dissolution-reprecipitation process. The high-resolution TEM (HRTEM) image (Fig. 3k) reveals that the lattice fringes with the distances of 0.351 nm and 0.367 nm, which match well with the *d*-spacings of (201) plane of HAP and (102) plane of Fe₂O₃. In addition, HRTEM image suggests good contact between HAP and Fe₂O₃, which would be feasible to the migration of photogenerated charges.

Fig. 4a demonstrates XRD patterns of Fe₂O₃, HAP/Fe₂O₃ and Co-HAP/Fe₂O₃ over FTO glass. The diffraction peaks of 2θ at 26.2°, 37.4°, 51.1°, and 61.4° match well with (110), (200), (211) and (310) planes of tetragonal SnO₂ (JCPDS No. 46-1088) from FTO substrate. The additional peaks at 35.2° and 64.8° are attributed to (110) and (300) planes of α phase Fe₂O₃ (JCPDS No.33-0664). After being decorated with HAP, the crystalline phase of Fe₂O₃ was well maintained; at the same time, new peaks with 2θ at 28.2° and 34.1° could suddenly be indexed to (102) and (202) planes of hexagonal HAP (JCPDS No.09-0432). The crystalline phase of HAP also well maintained after being ion-exchanged of Ca with Co, which might be attributed to the smaller size of Co²⁺ (72 pm) compared to that of Ca²⁺ (100 pm) [29]. The optical adsorption properties of Fe₂O₃, HAP/Fe₂O₃ and Co-HAP/Fe₂O₃ were investigated using UV-vis DRS (Fig. 4b). As shown, the absorption onset of Fe₂O₃ extends to approximately 590 nm, corresponding to 2.1 eV of the band gap for Fe₂O₃. After being deposited with HAP and Co-HAP, no significant changes on the absorption intensity and the absorption onset of Fe₂O₃ are observed, indicating HAP and Co-HAP have negligible impacts on light harvesting of Fe₂O₃.

X-ray photoelectron spectroscopy (XPS) was performed to investigate the chemical states of Fe₂O₃, HAP/Fe₂O₃ and Co-HAP/Fe₂O₃. The survey XPS spectra (Fig. S5a) identified the presence of Fe, O, Co, P and Ca in corresponding films. The absence of Fe2p in Fe₂O₃ at 711.2 and 724.5 eV suggests the surface of Fe₂O₃ is almost completely coated with HAP or Co-HAP (Fig. S5b). No significant difference of high resolution XPS spectra for Ca2p before and after the ion-exchange with Co indicates slight interaction between Ca and Co in HAP lattice (Fig. S5c). High resolution XPS spectra for Co2p in Co-HAP/Fe₂O₃ (Fig. 5a) shows two main peaks at binding energies of 781.2 and 797.2 eV, accompanied by two satellite bands at 785.6 and 802.9 eV respectively, are assigned to Co2p_{3/2} and Co2p_{1/2}. The peak separation of Co2p_{3/2} and Co2p_{1/2} is calculated to be *ca.* 16.0 eV, indicating Co is in the form of high-spin Co²⁺ state [30]. High resolution XPS spectra for O1s in all

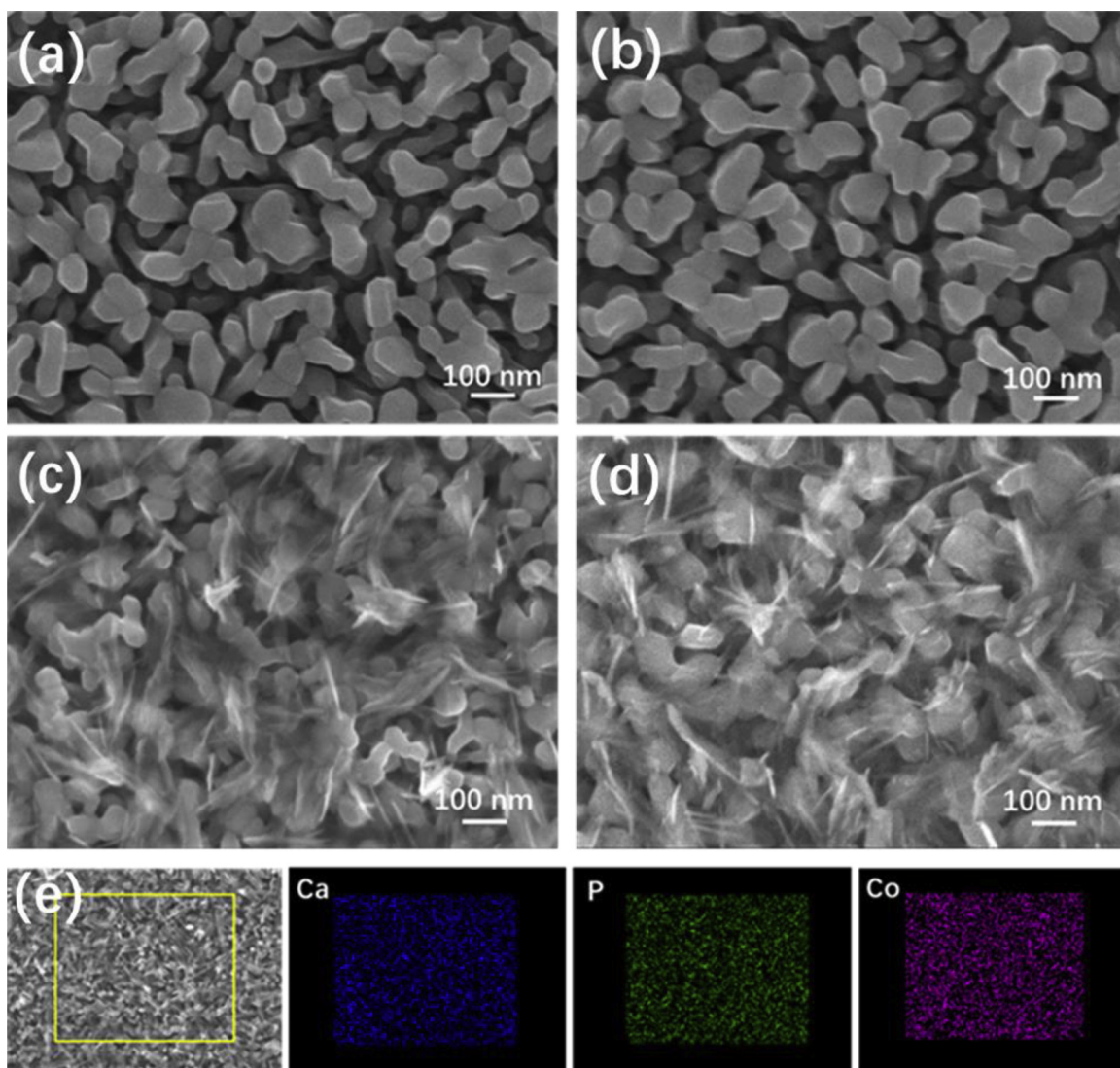


Fig. 2. SEM images of (a) Fe_2O_3 , (b) $\text{Ca}(\text{OH})_2/\text{Fe}_2\text{O}_3$, (c) HAP/ Fe_2O_3 , (d) Co-HAP/ Fe_2O_3 and (e) EDS mapping images of Ca, P and Co in Co-HAP/ Fe_2O_3 .

samples were highlighted in Fig. 5b by using Lorentzian-Gaussian fitting. For Fe_2O_3 , O1s was well fitted by two peaks at 529.7 and 531.1 eV, corresponding to the lattice oxygen and surface hydroxyl groups of Fe_2O_3 [13,31]. The peak for the lattice oxygen in Fe_2O_3 was not occurred in O1s profiles of HAP/ Fe_2O_3 and Co-HAP/ Fe_2O_3 , which might be owing to the complete shielding of Fe_2O_3 caused by HAP and Co-HAP layer. O1s for HAP/ Fe_2O_3 could be deconvoluted into two peaks at 532.3 and 530.7 eV, which could be assigned to O in hydroxyl groups ($\text{Ca}-\text{OH}$) and termination oxygen ($-\text{PO}_4^{3-}$), respectively [32]. The incorporation of Co obviously caused positive shifts of the binding energies of O1s in $\text{Ca}-\text{OH}$ and $-\text{PO}_4^{3-}$ by *ca.* 0.4 and 0.2 eV, indicating electronic modulations occurred in Co-HAP/ Fe_2O_3 . Such positive shift of O1s implied electron occupation of O was decreased, which would be beneficial to the electron transfer at the electrode/electrolyte interface and thus enhance water oxidation kinetics [33]. In addition, both peaks became slight broader, suggesting O existed in more than one coordination environment, like the hydroxyl groups ($\text{Ca}-\text{OH}$ and $\text{Co}-\text{OH}$) and the termination oxygen ($-\text{PO}_4^{3-}$). As further investigation, elemental composition of Co-HAP on Fe_2O_3 was determined by using inductively coupled plasma-atomic emission spectrometer (ICP-AES). The atomic ratio of Co/Ca was calculated to be *ca.* 0.31, indicating partial substitution of Ca by Co in HAP *via* ion-exchange process. Besides, $(\text{Co} + \text{Ca})/\text{P}$ was obtained as 1.46, which was lower than the

theoretical value of 1.67. This result implied that Co-HAP was non-stoichiometric with Ca deficiency and excess phosphate ions existed in Co-HAP/ Fe_2O_3 . According to literature, the deficiency of Ca could be compensated by the removal of OH- and thus produced OH- vacancies [34]. OH- vacancies could offer Lewis acidic sites, which could act as active sites for water adsorption and dissociation. On the other hand, excess phosphate ions adjacent to Fe_2O_3 surface would build a surface electric field, which would be beneficial for the separation and the transfer of photogenerated carries.

3.2. PEC performance of Co-HAP/ Fe_2O_3

Linear sweep voltammetry (LSV) curves were used to evaluate PEC performance Co-HAP/ Fe_2O_3 . Fig. 6a exhibits negligible currents for all HAP/ Fe_2O_3 in dark, while HAP/ Fe_2O_3 -2 shows the highest photocurrent density at a bias range of 0.92~1.40 V vs. RHE under illumination. With the increase of the deposition amount of HAP, the photocurrent density increases; while excessive HAP would result in photocurrent decrease, due to the insufficient transfer of photogenerated hole from Fe_2O_3 to electrode surface for subsequent water oxidation *via* a long migration distance. Unless otherwise specified, all the following investigations were based on HAP/ Fe_2O_3 -2 sample. It is also observed no cathodic shift on the onset potential, indicating HAP

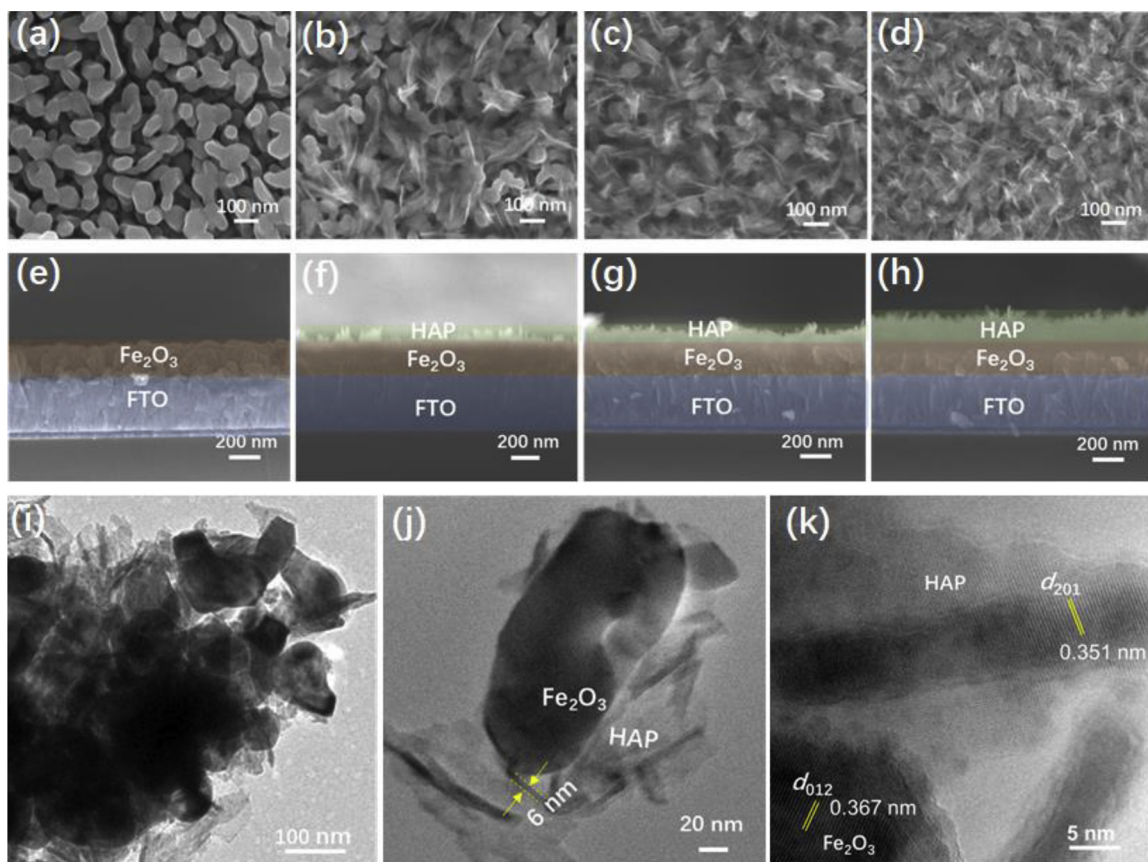


Fig. 3. Top and cross-sectional SEM images of (a, e) Fe_2O_3 , (b, f) HAP/ Fe_2O_3 -1, (c, g) HAP/ Fe_2O_3 -2 and (d, h) HAP/ Fe_2O_3 -3; and, TEM and HRTEM images of (i–k) HAP/ Fe_2O_3 .

presents no catalytic active sites for PEC water oxidation. It thus deduced the enhanced photocurrent caused by HAP was attributed to the improved charge separation and inhibited surface charge recombination. When partial Ca was substituted with Co, the photocurrent density of Co-HAP/ Fe_2O_3 was substantially increased to 2.25 mA cm^{-2} at 1.23 V vs. RHE, and a *ca.* 200 mV cathodic shift on onset potential comparing with that of Fe_2O_3 and HAP/ Fe_2O_3 (Fig. 6b). The lowest onset potential of $\sim 1.47 \text{ V}$ vs. RHE in dark also indicates Co-HAP/ Fe_2O_3 has superior OER activity than that of Fe_2O_3 and HAP/ Fe_2O_3 (Fig. S6). It also noted that, Co-HAP/ Fe_2O_3 -N only exhibited *ca.* one-sixth photocurrent density of Co-HAP/ Fe_2O_3 (Fig. S7), suggesting the pre-deposition of $\text{Ca}(\text{OH})_2$ followed by in-situ growth of HAP is essential to achieve highly efficient Co-HAP/ Fe_2O_3 . The OER performance of Co-HAP was further compared with that of CoPi, a well-known OER co-catalyst [28,35]. As seen from Fig. 6b, Co-HAP/ Fe_2O_3 exhibits a similar

onset potential for water oxidation to that of CoPi/ Fe_2O_3 , indicating Co species in Co-HAP probably undergo a similar oxidation path from Co (II) to Co(III) and/or Co(IV) by photogenerated holes prior to O_2 evolution. However, the photocurrent density of Co-HAP/ Fe_2O_3 (2.25 mA cm^{-2} at 1.23 V) is much higher than that of CoPi/ Fe_2O_3 (0.81 mA cm^{-2} at 1.23 V). The high OER efficiency of Co-HAP might be attributed to the highly dispersed Co sites, which could effectively act as active sites for water oxidation.

Fig. 6c displays the transient photocurrent responses of Fe_2O_3 , HAP/ Fe_2O_3 and Co-HAP/ Fe_2O_3 vs. time under the elevated potential with an interval of 0.2 V . Obviously, both anodic and cathodic photocurrent spikes appear upon light on/off. The anodic spike reflects the photogenerated holes transfer to the surface of photoanode and accumulate owing to the slow OER kinetics, while the cathodic spike represents the electrons flow back from encounter electrode *via* external circuit and

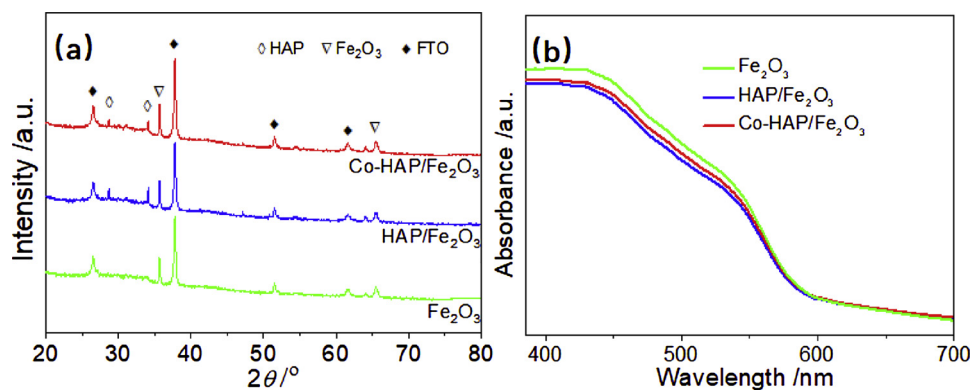


Fig. 4. (a) XRD patterns and (b) UV–vis absorption spectra of Fe_2O_3 , HAP/ Fe_2O_3 and Co-HAP/ Fe_2O_3 .

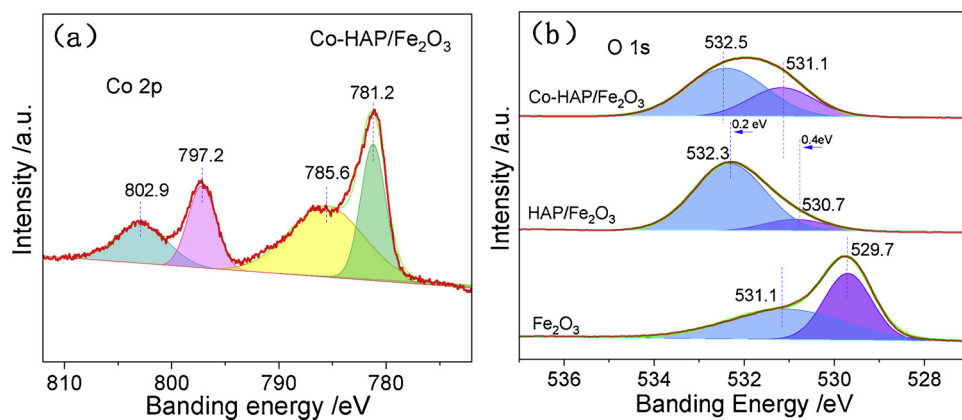


Fig. 5. XPS spectra of (a) Co 2p and (b) O 1s for Co-HAP/Fe₂O₃.

recombine with the accumulated holes on the surface [18,36]. Comparing with that of Fe₂O₃, HAP/Fe₂O₃ exhibits relatively lower height of anodic spike, which might be attributed to the slight inhibition of surface charge recombination; namely, HAP shows few passivation effect on Fe₂O₃ surface. When some Ca in HAP were substituted with Co, both anodic and cathodic spikes decreased intensively. Co(II) in Co-HAP might act as acceptor to capture holes from Fe₂O₃ surface to form Co(III/IV) species, which subsequently act as active sites for water oxidation. The acceptance for holes will benefit to improve the separation of photogenerated carries and simultaneously inhibit charge recombination. Furthermore, the water oxidation overpotential was decreased by transfer the reactive sites from Fe(IV) to Co(III/IV), thus facilitate the water oxidation kinetics. The applied bias to photo current conversion efficiency (ABPE) measured below thermodynamic

potential of water oxidation (*i.e.*, 1.23 V vs. RHE), from which the maximum photon to current conversion was achieved. As shown in Fig. 6d, ABPE for Co-HAP/Fe₂O₃ shows a maximum value of 0.25% at 1.0 V vs. RHE, significantly superior to 0.06% at 1.10 V of HAP/Fe₂O₃ and 0.016% at 1.10 V of Fe₂O₃. The enhanced efficiency further confirms Co-HAP over Fe₂O₃ could not only facilitate the charge separation but also promote water oxidation kinetics.

The PEC stability of Co-HAP/Fe₂O₃ was further examined a bias of 1.23 V vs. RHE, as well as that of Fe₂O₃, HAP/Fe₂O₃ and CoPi/Fe₂O₃. As shown in Fig. 7a, the photocurrent density of Fe₂O₃ decays to ~70% within 2 h, owing to poor stability in neutral electrolyte. In contrast, HAP/Fe₂O₃ exhibits a long-term stability, indicating HAP layer could act as an efficient protector to inhibit the hydrolysis of Fe₂O₃. HAP layer could not only inhibit the arrival of proton on Fe₂O₃ but also

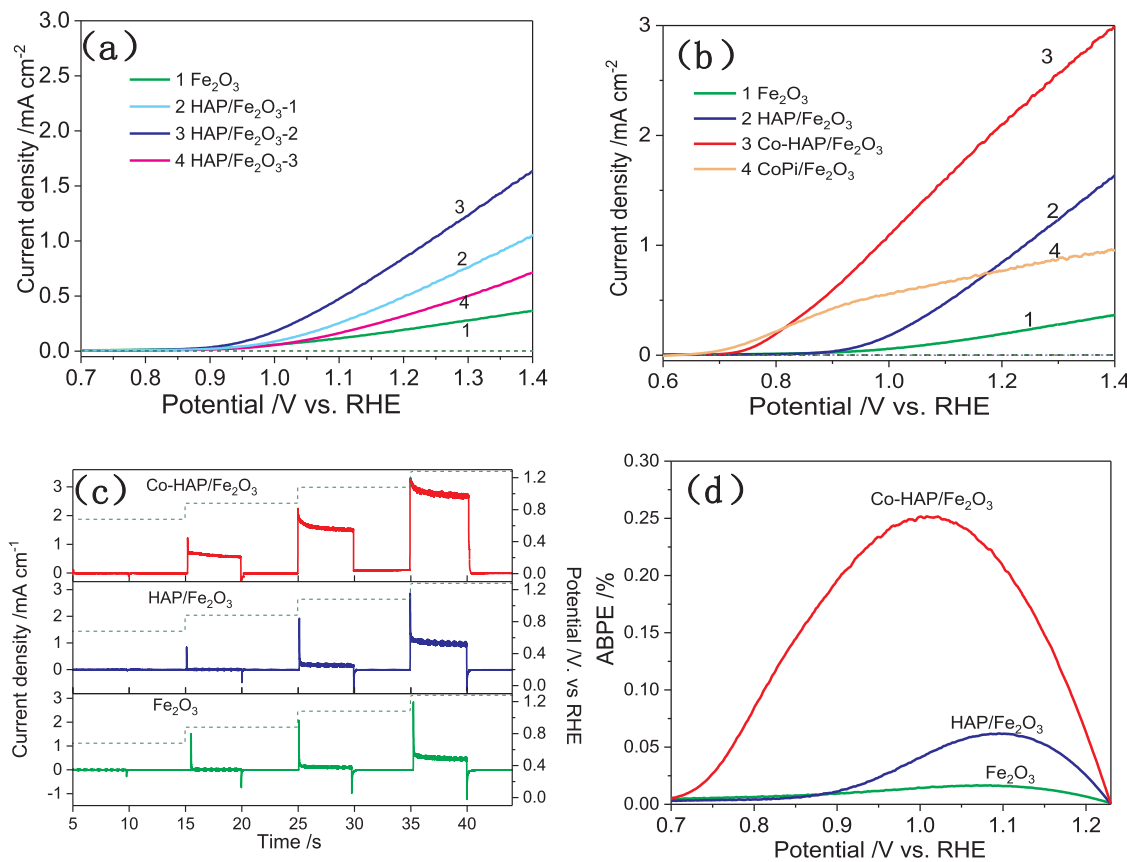


Fig. 6. (a and b) LSV curves and (c) chronoamperometry photocurrent (solid line) under stepped potential (dash line) of Fe₂O₃, HAP/Fe₂O₃ and Co-HAP/Fe₂O₃ photoanodes; (d) ABPE of Fe₂O₃, HAP/Fe₂O₃ and Co-HAP/Fe₂O₃ as a function of applied potential. Dash lines in (a) and (b) represent LSV curves tested in dark.

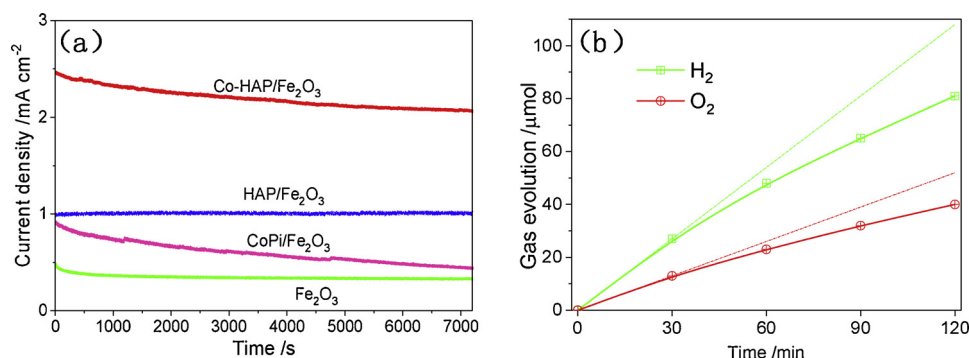


Fig. 7. (a) Amperometric i - t curves of Fe_2O_3 , $\text{HAP}/\text{Fe}_2\text{O}_3$ and $\text{Co-HAP}/\text{Fe}_2\text{O}_3$ at 1.23 V vs. RHE. (b) Time course of PEC H_2 and O_2 evolution over $\text{Co-HAP}/\text{Fe}_2\text{O}_3$ (ca. 4.0 cm^2) at 1.23 V vs. RHE.

could mediate the transfer of produced proton into electrolyte by the counter-ions (OH^- or PO_4^{3-}). However, $\text{Co-HAP}/\text{Fe}_2\text{O}_3$ shows a slightly satisfactory PEC stability with $\sim 75\%$ remain of the initial photocurrent density in 2 h, which is comparable to that of $\text{CoPi}/\text{Fe}_2\text{O}_3$. The photocurrent decay might result from the slow water oxidation kinetics, which leads to much more hole accumulation over Co-HAP. After the acceptance of holes, Co(II) species are changed into Co(III) and/or Co(IV) species, which would cause the change on the lattice structure and subsequently the degradation of Co-HAP, or the formation of the poor active CoO_x species [23,37]. PEC water splitting of $\text{Co-HAP}/\text{Fe}_2\text{O}_3$ was measured by the determination of H_2 evolution and O_2 evolution at a bias of 1.23 V vs. RHE. The accumulated H_2 evolution and O_2 evolution within 2 h irradiation were plotted in Fig. 7b. The initial H_2 and O_2 evolution rates at first 30 min were calculated to be 47.2 and $22.5 \mu\text{mol h}^{-1}$, respectively. However, an obvious decay for H_2 and O_2 generation was observed with the prolonged time, which is agreement with PEC stability test. It is therefore highly desired to further improve the PEC stability of such photoanode *via* various strategies, for example the optimization of the lattice structure of HAP by substituting Ca and/or OH^- with other cations and/or ions. Moreover, the further improvement of water oxidation kinetics on Co-HAP are also expected.

3.3. Mechanism analysis

PEC water oxidation reaction occurs at the active sites on the surface of electrode; the increase of surface active sites is often primarily responsible for enhanced catalytic activity. The origin for the enhanced OER was therefore evaluated by comparing the electrochemically active surface area (ECSA), which could be estimated from the electrochemical double-layer capacitance (C_{dl}) by measuring cyclic voltammograms (CVs) in a non-Faradaic region. The detailed CVs for Fe_2O_3 , $\text{HAP}/\text{Fe}_2\text{O}_3$ and $\text{Co-HAP}/\text{Fe}_2\text{O}_3$ were recorded in the potential range of 0.56–0.86 V vs. RHE with various scan rates and shown in Fig. 8a-c. The C_{dl} was then calculated by the equation $C_{dl} = i_c/v$ [38], where i_c represents the capacity current density at 0.66 V vs. RHE and v is the scanning rate. The fitting linearity of i_c against v were plotted in Fig. 8d. As seen, C_{dl} for $\text{Co-HAP}/\text{Fe}_2\text{O}_3$ (0.13 m F cm^{-2}) is significantly larger than that for $\text{HAP}/\text{Fe}_2\text{O}_3$ ($0.065 \text{ m F cm}^{-2}$) and Fe_2O_3 ($0.051 \text{ m F cm}^{-2}$). This result indicates $\text{Co-HAP}/\text{Fe}_2\text{O}_3$ has higher intrinsic catalytic activity. Taking the similar surface morphology into account, Co in $\text{Co-HAP}/\text{Fe}_2\text{O}_3$ was speculated to play critical roles that increased ECSA for water oxidation over electrode surface.

Except for ESCA, charge transfer dynamics at electrode/electrolyte interface is also an important factor in catalysis process. To gain insight into the charge transfer dynamics, electrochemical impedance spectroscopy (EIS) based on Fe_2O_3 , $\text{HAP}/\text{Fe}_2\text{O}_3$ and $\text{Co-HAP}/\text{Fe}_2\text{O}_3$ were conducted and shown in Fig. 9a. The experimental data are fitted using the equivalent circuit (Fig. 9b), in which R_s is the series resistance consisted of FTO resistance and contact resistance, R_{CT} represents the

charge transfer resistance at the electrode/electrolyte interface, and CPE is constant phase element, corresponding to the interfacial chemical capacitance [39]. R_{CT} value for $\text{HAP}/\text{Fe}_2\text{O}_3$ was calculated as 1045Ω , which is significantly smaller than that of Fe_2O_3 (2433Ω), indicating the fast charge transfer from $\text{HAP}/\text{Fe}_2\text{O}_3$ into electrolyte. In other words, HAP promotes the charge transfer kinetics at electrode/electrolyte interface. The improvement on charge transfer might be attributed to the hydroxyl ion channels of hexagonal HAP, which facilitates the charge carrier migration [40,41]. After Co was incorporated, R_{CT} value was further reduced to 507Ω , suggesting Co sites in $\text{Co-HAP}/\text{Fe}_2\text{O}_3$ further accelerated the water oxidation kinetics over the electrode surface.

To further reveal the effect of Co-HAP on PEC performance of Fe_2O_3 , the charge separation efficiency in bulk (η_{bulk}) and the charge transfer efficiency on the surface ($\eta_{surface}$) were investigated by using H_2O_2 as a hole scavenger. Due to H_2O_2 possesses a rapider oxidation rate and a lower overpotential than that of H_2O , the photocurrent density in the presence of H_2O_2 could represent the number of separated charges, which successfully reach the electrode surface without recombination in bulk [36]. The photocurrent densities for Fe_2O_3 , $\text{HAP}/\text{Fe}_2\text{O}_3$ and $\text{Co-HAP}/\text{Fe}_2\text{O}_3$ in the presence or absence of H_2O_2 in electrolyte were shown in Fig. S8. Accordingly, η_{bulk} and $\eta_{surface}$ are illustrated in Fig. 10. It is obvious that both η_{bulk} and $\eta_{surface}$ exhibit an order of $\text{Co-HAP}/\text{Fe}_2\text{O}_3 > \text{HAP}/\text{Fe}_2\text{O}_3 > \text{Fe}_2\text{O}_3$ in the whole potential range of 0.9–1.6 V vs. RHE. Typically, η_{bulk} values for $\text{Co-HAP}/\text{Fe}_2\text{O}_3$ (ca. 36.1%) and $\text{HAP}/\text{Fe}_2\text{O}_3$ (ca. 30.8%) at 1.23 V vs. RHE are significantly higher than that of bare Fe_2O_3 (15.3%). Such improvement on η_{bulk} might be attributed to the formation of a negative electrostatic field by the surface anchored PO_4^{3-} (from HAP) on Fe_2O_3 [42,43]. The electrostatic field is beneficial to the extraction of photogenerated holes from bulk Fe_2O_3 to surface, thus enhanced the charge separation in bulk. Being different from that of η_{bulk} , $\eta_{surface}$ of $\text{Co-HAP}/\text{Fe}_2\text{O}_3$ exhibits the highest value of 88.1% (at 1.23 V vs. RHE), which is ca. 2.65 and 7.10 times that of $\text{HAP}/\text{Fe}_2\text{O}_3$ (33.2%) and Fe_2O_3 (12.4%) respectively. Due to the versatile structure of HAP, H_2O could be adsorbed on Lewis acidic sites (Ca^{2+}) and simultaneously bonded to Lewis basic sites (O^{2-} in PO_4^{3-} and OH^-) *via* H atom, which would promote the activation/dissociation of H_2O and thus facilitate the water oxidation [44]. The larger difference in $\eta_{surface}$ with similar η_{bulk} between $\text{Co-HAP}/\text{Fe}_2\text{O}_3$ and $\text{HAP}/\text{Fe}_2\text{O}_3$ indicates the role of Co is to enhance the surface charge transfer to water molecular; in other word, Co inhibits the surface charge recombination. As previous report, Co(II) specie would act as acceptor to capture hole to form higher valence states Co(III) and/or Co(IV), thus suppress the charge recombination.

Based on the above analysis, it can be concluded Fe_2O_3 could generate electron-hole pairs under illumination; however, it suffers from the serious bulk and surface charge recombination, due to its intrinsic deficiency (such as low conductivity, short electron diffusion length and so on) and the sluggish surface water oxidation kinetics (the lowest η_{bulk}

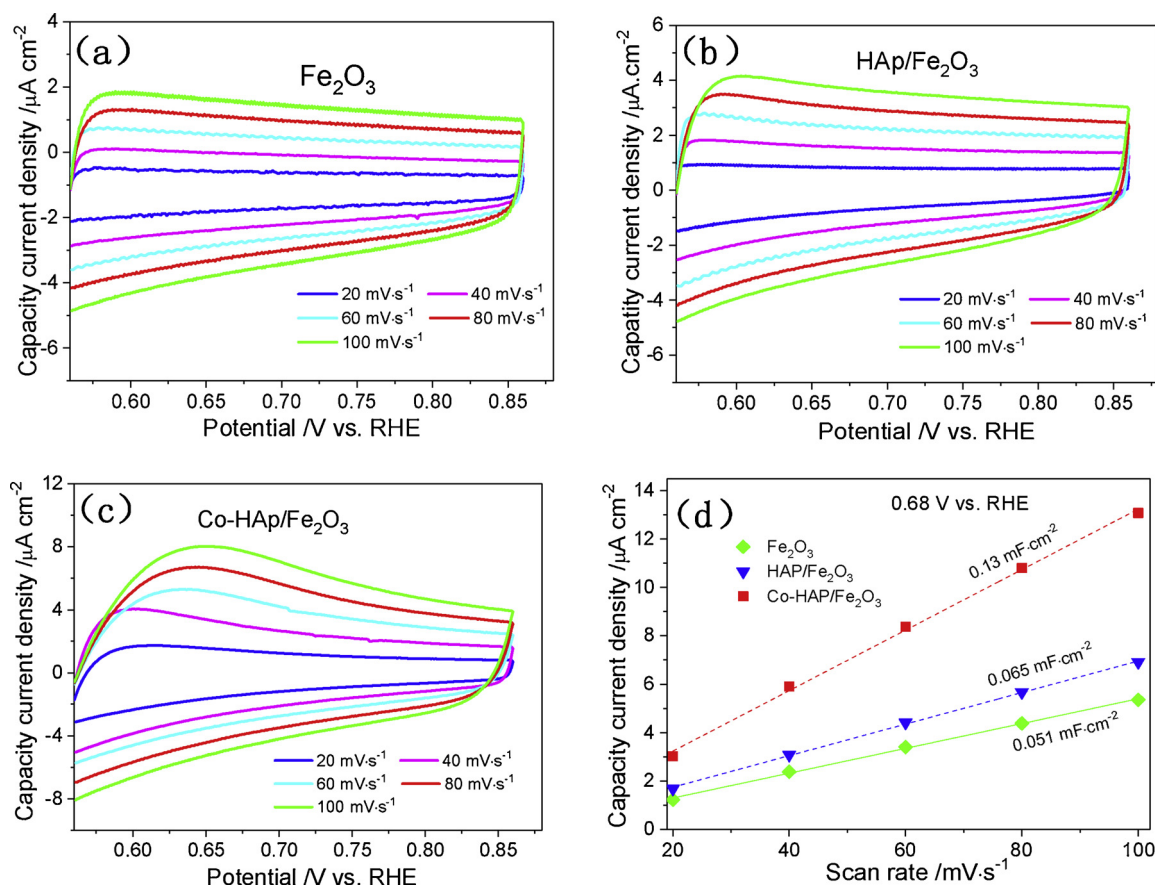


Fig. 8. Cyclic voltammograms (CVs) for (a) Fe_2O_3 , (b) $\text{HAp/Fe}_2\text{O}_3$ and (c) $\text{Co-HAp/Fe}_2\text{O}_3$ at five different scan rates; and, (d) The linear relationship of the capacity current at 0.68 V vs. RHE against scan rates for various photoanodes. The CVs were conducted in non-Faradaic potential range from 0.56 to 0.86 V vs. RHE at scan rates of 20, 40, 60, 80 and 100 mV s^{-1} .

and the lowest η_{surface}). The modification with HAP would enhance the charge separation in bulk of Fe_2O_3 (the higher η_{bulk}), but it still suffers from the sluggish surface water oxidation, which makes the surface accumulated holes recombine with electrons and results in “kinetic bottleneck” phenomenon over $\text{HAp/Fe}_2\text{O}_3$. Owing to the incorporation of Co, the surface charges (holes) are efficiently transferred to water molecular (the highest η_{surface}). On the other hand, the abundant Lewis acidic and Lewis basic sites of HAP promote the activation/dissociation of H_2O (the enhanced η_{surface} of $\text{HAp/Fe}_2\text{O}_3$), which is beneficial for water oxidation reaction. Thus, the Co incorporation and the versatile HAP structure are indispensable for achieving highly efficient oxygen

evolution cocatalyst (Co-HAP) over photoanode surface, like Fe_2O_3 . Fig. 11 schematically illustrated the overall process of water oxidation over $\text{Co-HAp/Fe}_2\text{O}_3$. Under illumination, Fe_2O_3 was excited by photo to generated electron-hole pairs and subsequently separated to electrons and holes. The electrons were then migrated via an external circuit to Pt counter electrode, where water was reduced to produce H_2 . At the same time, the holes in bulk Fe_2O_3 migrated to Fe_2O_3 surface with the assistance of interfacial PO_4^{3-} groups and further to Co-HAP nanostructures, where the holes were capture by Co(II) to produce Co(III) and/or Co(IV). On the other hand, H_2O was diffused to HAP surface, where H_2O was activated by interaction with Lewis acidic and Lewis

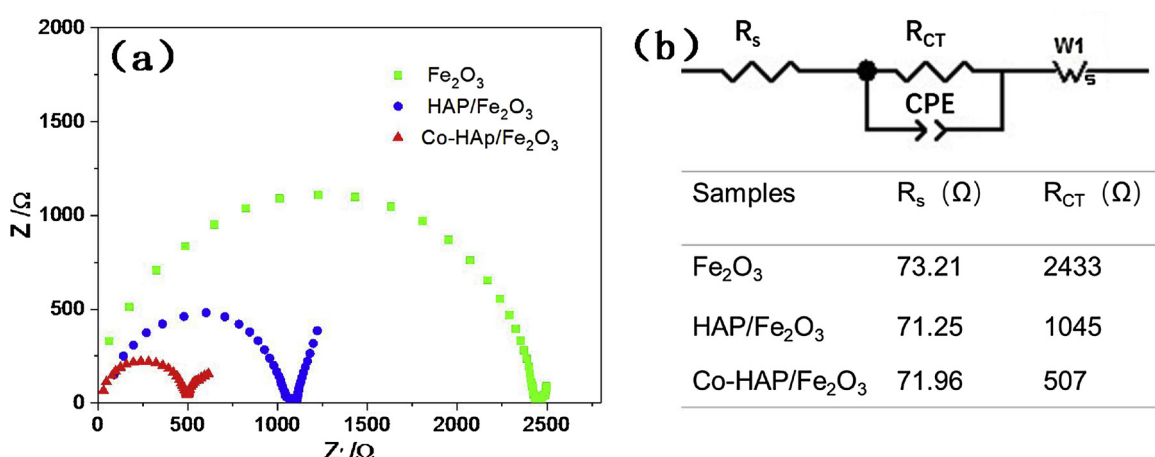


Fig. 9. (a) EIS of Fe_2O_3 , $\text{HAp/Fe}_2\text{O}_3$ and $\text{Co-HAp/Fe}_2\text{O}_3$; and, (b) the equivalent circuit and corresponding parameters.

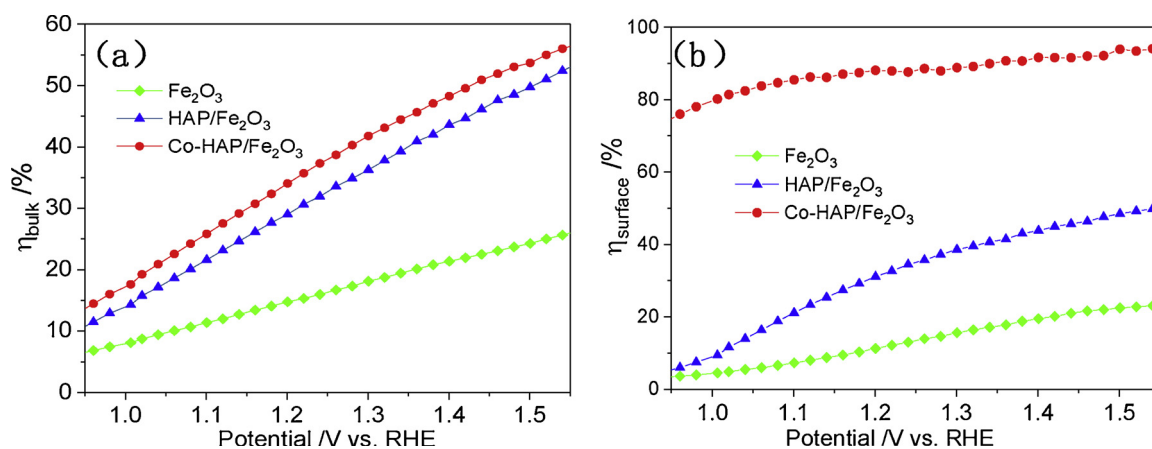


Fig. 10. (a) η_{bulk} and (b) η_{surface} of Fe_2O_3 , $\text{HAP}/\text{Fe}_2\text{O}_3$ and $\text{Co-HAP}/\text{Fe}_2\text{O}_3$ photoanodes.

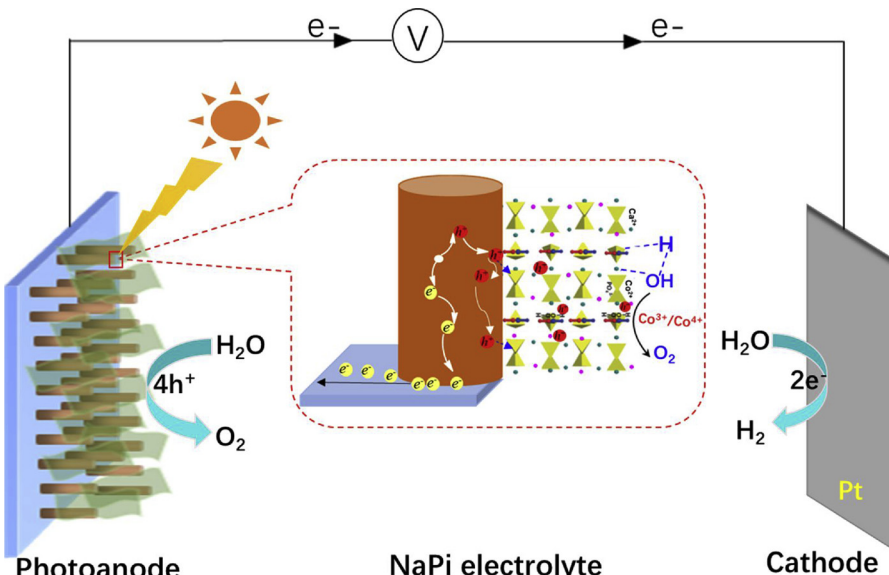


Fig. 11. Schematic mechanism for Co-HAP boosting PEC water oxidation over Fe_2O_3 .

basic sites. The activated H_2O was finally oxidized by adjacent Co(III) and/or Co(IV) to produce O_2 via a multi-step reaction. As a result, Co-HAP exhibits excellent performance for boosting PEC water splitting over Fe_2O_3 photoanode.

4. Conclusion

In summary, we have designed and fabricated a novel OER cocatalyst Co-incorporated HAP, which was decorated on the surface of Fe_2O_3 nanoarrays by a successive in-situ deposition, in-situ growth and ionic-exchange process. The optimized Co-HAP/ Fe_2O_3 exhibits an outstanding PEC water oxidation, even superior to the well-known CoPi, with a photocurrent density of 2.25 mA cm^{-2} at 1.23 V vs. RHE in neutral electrolyte, which is *ca.* 9.78 times that of bare Fe_2O_3 , and a $\sim 200 \text{ mV}$ cathodic shift of the onset potential. The enhanced PEC activity of Co-HAP/ Fe_2O_3 is attributed to the following factors: 1) The interfacial PO_4^{3-} from Co-HAP is beneficial to the extraction of photo-generated holes from bulk Fe_2O_3 to surface; that is, the charge separation efficiency of Fe_2O_3 is enhanced with the assistance of interfacial PO_4^{3-} groups; 2) Co in Co-HAP plays a critical role as active sites to improve surface charge transfer via the capture of photogenerated holes, which are subsequently used for water oxidation; and, 3) 2D nanostructure allows for efficient charge transfer and water absorption, as well as the abundant Lewis acidic and Lewis basic sites in Co-HAP.

facilitates the activation/dissociation of H_2O , thus benefits the water oxidation process. Though more efforts are expected to further improve the PEC stability of Co-HAP/ Fe_2O_3 , Co-HAP here has presented great potential as a novel OER cocatalyst to boost PEC water splitting over semiconductor-based anodes. Moreover, the strategy for fabrication of Co-HAP should be applicable to many newly 2D OER catalysts, opening a new path in this urgent field of energy conversion.

Acknowledgements

The work was supported by the National Natural Science Foundation of China (51502078), the Major Project of Science and Technology, Education Department of Henan Province (17B610003, 19A150018 and 19A150019), Henan University (YQPY20170013), the program for Science & Technology Innovation Team in Universities of Henan Province (19IRTSTHN029).

Appendix A. Supplementary data

Supplementary material related to this article can be found, in the online version, at doi:<https://doi.org/10.1016/j.apcatb.2019.03.038>.

References

[1] A. Landman, H. Dotan, G.E. Shter, M. Wullenkord, A. Houaijia, A. Maljusch, G.S. Grader, A. Rothschild, *Nat. Mater.* 16 (2017) 646.

[2] S.Y. Reece, J.A. Hamel, K. Sung, T.D. Jarvi, A.J. Esswein, J.J.H. Pijpers, D.G. Nocera, *Science* 334 (2011) 645–648.

[3] M.P. Suryawanshi, U.V. Ghorpade, S.W. Shin, U.P. Suryawanshi, H.J. Shim, S.H. Kang, J.H. Kim, *Small* 14 (2018) 1801226.

[4] D.K. Zhong, S. Choi, D.R. Gamelin, *J. Am. Chem. Soc.* 133 (2011) 18370–18377.

[5] S. Kevin, V.D.K. Roel, *Nat. Rev. Mater.* 1 (2016) 15010.

[6] J. Seo, H. Nishiyama, T. Yamada, K. Domen, *Angew. Chem. Int. Edit.* 57 (2018) 8396–8415.

[7] J. Gan, X. Lu, Y. Tong, *Nanoscale* 6 (2014) 7142–7164.

[8] C. Li, Z. Luo, T. Wang, J. Gong, *Adv. Mater.* (2018) 30.

[9] K. Sivula, F. Le Formal, M. Graetzel, *ChemSusChem* 4 (2011) 432–449.

[10] S. Shen, S.A. Lindley, X. Chen, J.Z. Zhang, *Energ. Environ. Sci.* 9 (2016) 2744–2775.

[11] P. Kuang, L. Zhang, B. Cheng, J. Yu, *Appl. Catal. B-Environ.* 218 (2017) 570–580.

[12] A.K. Singh, D. Sarkar, *Nanoscale* 10 (2018) 13130–13139.

[13] F. Li, J. Li, F. Li, L. Gao, X. Long, Y. Hu, C. Wang, S. Wei, J. Jin, J. Ma, *J. Mater. Chem. A* 6 (2018) 13412–13418.

[14] R. Zhang, L. Yang, X. Huang, T. Chen, F. Qu, Z. Liu, G. Du, A.M. Asiri, X. Sun, *J. Mater. Chem. A* 5 (2017) 12086–12090.

[15] X. Bu, Y. Gao, S. Zhang, Y. Tian, *Chem. Eng. J.* 355 (2019) 910–919.

[16] D. Li, J. Shi, C. Li, *Small* 14 (2018) 1704179.

[17] J. Yang, D. Wang, H. Han, C. Li, *Acc. Chem. Res.* 46 (2013) 1900–1909.

[18] Z. Wang, G. Liu, C. Ding, Z. Chen, F. Zhang, J. Shi, C. Li, *J. Phys. Chem. C* 119 (2015) 19607–19612.

[19] P. Dias, L. Andrade, A. Mendes, *Nano Energy* 38 (2017) 218–231.

[20] R. Chong, Z. Wang, J. Li, H. Han, J. Shi, C. Li, *RSC Adv.* 4 (2014) 47383–47388.

[21] R. Chong, B. Wang, C. Su, D. Li, L. Mao, Z. Chang, L. Zhang, *J. Mater. Chem. A* 5 (2017) 8583–8590.

[22] G. Liu, Y. Zhao, R. Yao, N. Li, M. Wang, H. Ren, J. Li, C. Zhao, *Chem. Eng. J.* 355 (2019) 49–57.

[23] Y. Ma, A. Kafizas, S.R. Pendlebury, F. Le Formal, J.R. Durrant, *Adv. Funct. Mater.* 26 (2016) 4951–4960.

[24] L. Silvester, J. Lamonier, R. Vannier, C. Lamonier, M. Capron, A. Mamede, F. Pourpoint, A. Gervasini, F. Dumeignil, *J. Mater. Chem. A* 2 (2014) 11073–11090.

[25] G. Xu, J. Guo, Y. Zhang, Y. Fu, J. Chen, L. Ma, Q. Guo, *ChemCatChem* 7 (2015) 2485–2492.

[26] S.P. Thanh, A.R. Sane, B.R. de Vasconcelos, A. Nzihou, P. Sharrock, D. Grouset, P.M. Doan, *Appl. Catal. B Environ.* 224 (2018) 310–321.

[27] G. Wang, B. Wang, C. Su, D. Li, L. Zhang, R. Chong, Z. Chang, *J. Catal.* 359 (2018) 287–295.

[28] D.K. Zhong, M. Cornuz, K. Sivula, M. Graetzel, D.R. Gamelin, *Energy Environ. Sci.* 4 (2011) 1759–1764.

[29] D.C. Carvalho, L.G. Pinheiro, A. Campos, E.R.C. Millet, F.F. de Sousa, J.M. Filho, G.D. Saraiva, E.C. Da Silva Filho, M.G. Fonseca, A.C. Oliveira, *Appl. Catal. A Gen.* 471 (2014) 39–49.

[30] J. Guan, C. Ding, R. Chen, B. Huang, X. Zhang, F. Fan, F. Zhang, C. Li, *Chem. Sci.* 8 (2017) 6111–6116.

[31] W. Liu, H. Liu, L. Dang, H. Zhang, X. Wu, B. Yang, Z. Li, X. Zhang, L. Lei, S. Jin, *Adv. Funct. Mater.* (2017) 27.

[32] C. Viorney, Y. Chevrolot, D. Léonard, B.R. Aronsson, P. Péchy, H.J.R. Mathieu, P. Descouts, M. Grätzel, *Langmuir* 18 (2002) 2582–2589.

[33] B. Zhang, Y.H. Lui, H. Ni, S. Hu, *Nano Energy* 38 (2017) 553–560.

[34] L. Silvester, J. Lamonier, R. Vannier, C. Lamonier, M. Capron, A. Mamede, F. Pourpoint, A. Gervasini, F. Dumeignil, *J. Mater. Chem. A* 2 (2014) 11073–11090.

[35] D.K. Zhong, D.R. Gamelin, *J. Am. Chem. Soc.* 132 (2010) 4202–4207.

[36] D.K. Zhong, S. Choi, D.R. Gamelin, *J. Am. Chem. Soc.* 133 (2011) 18370–18377.

[37] H.W. Jeong, T.H. Jeon, J.S. Jang, W. Choi, H. Park, *J. Phys. Chem. C* 117 (2013) 9104–9112.

[38] C.C.L. Mccrory, S. Jung, I.M. Ferrer, S.M. Chatman, J.C. Peters, T.F. Jaramillo, *J. Am. Chem. Soc.* 137 (2015) 4347–4357.

[39] D. Chen, Z. Liu, *ChemSusChem* 11 (2018) 3438–3448.

[40] M.B. Suresh, P. Biswas, V. Mahender, R. Johnson, *Mater. Sci. Eng. C Mater.* 70 (2017) 364–370.

[41] X. Fu, J. Wang, D. Huang, S. Meng, Z. Zhang, L. Li, T. Miao, S. Chen, *ACS Catal.* 6 (2016) 957–968.

[42] K. Liu, H. Wang, Q. Wu, J. Zhao, Z. Sun, S. Xue, *J. Power Sources* 283 (2015) 381–388.

[43] J.Y. Kim, J. Jang, D.H. Youn, G.M. Lee, J.S. Lee, *Adv. Energy Mater.* 4 (2014) 1400476.

[44] R. Chong, Y. Fan, Y. Du, L. Liu, Z. Chang, D. Li, *Int. J. Hydro. Energy* 43 (2018) 22329–22339.